AIAA JOURNAL
Vol. 33, No. 4, April 1995

Validation of Code Using Turbulence Model Applied to Three-Dimensional Transonic Channel

Juliette Cahen*
Société Nationale d'Etude et de Construction de Moteurs d'Aviation, 77550 Moissy-Cramayel, France
and
Vincent Couaillier,† Jean Délery,‡ and Thierry Pot§
ONERA, 92320 Châtillon, France

The flow induced by a swept bump mounted on the lower wall of a transonic channel has been thoroughly analyzed on the basis of surface pressure measurements, surface flow visualizations, and field measurements by a three-component laser Doppler velocimeter system. The same flow has been computed by a code solving the full time-averaged Navier–Stokes equations by a method using an explicit centered finite difference scheme applied to a finite volume approach. An algebraic model using the mixing length concept and the Jones-Launder $[k, \epsilon]$ transport equation model have been considered. Both models give a faithful prediction of the essential features of the flow; in particular, the shock pattern forming in the channel is well predicted. However, the $[k, \epsilon]$ model shows a clear superiority in the prediction of the behavior of the interacting dissipative layers.

Introduction

INTERACTIONS between the boundary layers and the shock waves forming in a three-dimensional supersonic or transonic channel always have detrimental effects on the aerodynamics performance of the system, whether it is an air intake, a nozzle, a diffusor, or a compressor cascade. Such interactions lead to important losses in terms of efficiency—or pressure recovery—and, if separation occurs, they are frequently at the origin of unsteady phenomena which can be extremely harmful. Much has been said about two-dimensional (planar or axisymmetric) shock wave/boundary-layer interactions, the physical properties of which can be considered as well understood.[1] To treat these kinds of problems, design engineers can rely on a large number of experimental results providing scaling laws for the interaction extent as well as criteria to define the limit for shock induced separation. Furthermore, rather reliable predictive methods have been developed using various theoretical approaches.[2–7]

However, the large majority of practical configurations being three-dimensional, a large effort is presently being made devoted to the study of three-dimensional interactions to arrive at a clear physical understanding of these flows, the structure of which can be far more involved than in two-dimensional flows,[8,9] and to develop numerical tools to treat complex three-dimensional geometries. Indeed, calculation of three-dimensional flows, including more or less extended separated zones, must call on the solution of the full time-averaged Navier–Stokes equations. However, independent of the question of computer cost, this approach still leads to severe numerical problems both to properly capture the flow features and to accurately predict its essential properties. In addition, the definition of realistic turbulence models remains a major issue in the calculation of massively separated flows.

The objective of the present study was to analyze in depth the field resulting from multiple shock wave/boundary layer interactions occurring in a three-dimensional transonic channel. In this case, the interactions taking place with the boundary layers of the four walls can lead to the formation of several separations which are at the origin of vortical structures cause of intense secondary flows. Firstly, a basic experiment has been executed aiming at a thorough description of the flowfield to arrive at a clear understanding of its structure and to provide a well-documented test case. Secondly, Navier–Stokes calculations have been performed on the same configuration to assess the accuracy of the numerical method and to validate the turbulence models by comparison with the results of the experiment. The present study is a considerable extension of previous work in which the same geometry was considered.[10,11] Progress made since that time has allowed both a more complete experimental investigation of the flowfield and an execution of more advanced calculations.

Tested Configuration and Experimental Techniques

Definition of the Channel

The geometrical definition of the tested channel is shown in Fig. 1. It consists of a converging-diverging section with three flat faces and the fourth face (lower wall) bearing a swept bump. The test section is 120 mm wide and 100 mm high in the inlet plane. The upstream part of the bump is flat and inclined at 7 deg with respect to the horizontal. This first portion is followed by a contour of variable slope, beginning with a circular convex part with a 100 mm radius of curvature, followed by a concave circular part with a radius of 180 mm. The two circular arcs are defined so as to insure slope continuity at the points where they interconnect as well as at the points where they come to contact with the rectilinear upstream and downstream parts.

The three-dimensional effect is achieved by sweeping the bump crest line 30 deg from the upstream flow direction. The maximum height of the bump is 20 mm and its length is equal to 355 mm. The generation is cylindrical downstream of the crest line (see Ref. 12 for a more complete definition of the channel geometry). The incoming subsonic flow accelerates in the converging part of the channel to reach a sonic state in the vicinity of the bump crest, which constitutes a throat. The flow becomes supersonic downstream and then, because of the choking effect caused by an adjustable second throat, it decelerates through shock waves interacting strongly with the boundary layers of the channel walls. The test setup is installed in a continuous wind tunnel supplied with dessicated atmospheric air under a stagnation pressure $p_{st} = 92{,}000$ Pa and a stagnation temperature $T_{st} = 300$ K. The Reynolds number computed with the sonic state and using the throat height (80 mm) as the reference length is 11.3×10^5. Under these conditions, the boundary layers are fully turbulent well upstream of the interactions.

Presented as Paper 93-0293 at the AIAA 31st Aerospace Sciences Meeting, Reno, NV, Jan. 11–14, 1993; received Sept. 1, 1993; revision received Sept. 29, 1994; accepted for publication Sept. 30, 1994.

*Ph.D. Student, Aerodynamics Department.
†Research Group Leader, Aerodynamics Department. Member AIAA.
‡Research Division Head, Aerodynamics Department. Member AIAA.
§Technical Engineer, Aerodynamics Department.

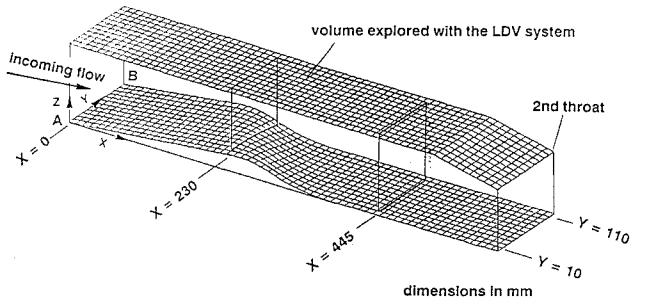

Fig. 1 Geometrical definition of the three-dimensional transonic channel.

Means of Investigation

The four channel walls were equipped with a total of 597 pressure orifices, 216 installed on the lower wall bearing the bump, 181 on the top wall, and 100 on each side wall (for the pressure measurements, the side windows were replaced by metal plates equipped with the pressure tapping). The skin-friction line patterns on the four faces of the channel were visualized by the oil-film technique. The field measurements were executed by using a three-component laser Doppler velocimeter (LDV) system working in the forward scattering mode.[13] This velocimeter is equipped with two identical 15-W argon lasers. The first operates in single-line violet (wave length ($\lambda = 0.4765$ μm) at a power of 3 W. The second is used in an all-line mode at 6 W, with the beam split by a set of dichroic mirrors into two colors, green ($\lambda = 0.5145$ μm) and blue ($\lambda = 0.4880$ μm). The three pairs of beams are focused by an appropriate lens system to constitute the probe volume, the useful diameter of which is 200 μm. In the present arrangement, the blue and green beams are emitted in a horizontal plane at an angle of -24 deg with respect to the Y spanwise axis. The violet component is also emitted in a horizontal plane but at an angle of $+25$ deg with respect to the Y axis. The velocity vector is thus measured in a system of axes in which one axis (Z) is vertical and the two others (X_1 and X_2) lie in a horizontal plane 49 deg from each other. Elementary formulas can then convert these velocity components into the wind tunnel (X, Y, Z) coordinate system in which the results are expressed (see Fig. 1).

For the velocimeter to determine the orientation of the measured velocity components, the six beams traverse Bragg cells inducing a shift of the fringes corresponding to a frequency of 10 MHz for the three colors. The collecting part includes two Cassegrain telescopes, with a diameter of 200 mm. The light from the first of these telescopes passes through interference filters which select the green and blue components. The second telescope selects the violet in the same way. The separated components are applied to three photomultipliers whose signals are processed by DANTEC type 55L counters connected to the acquisition system.

To achieve an acceptable acquisition rate, especially in the separated regions, the flow was seeded with paraffin droplets injected through a tube in the wind-tunnel settling chamber. At each measurement station, the three components of the instantaneous velocity were acquired on a sample of 2000 events corresponding to 2000 particles crossing the probe volume, hence a total of $3 \times 2000 = 6000$ instantaneous values of the U, V, and W components along the X, Y, and Z axes, respectively. The various statistical moments—mean values, standard deviations, cross correlations—were computed from this sample. The second-order moments are identified with the Reynolds tensor components. The volume explored with the LDV system is represented in Fig. 1. The measurements have been executed along 220 vertical stations contained in 11 longitudinal planes, each comprising 96 points, hence a total of 21,120 measurement points.

Numerical Method and Turbulence Models

Governing Equations

The flow is represented by the compressible time-averaged Navier–Stokes equations associated with a turbulence model. The flow governing equations can be written in the following compact form:

$$\frac{\partial \boldsymbol{f}}{\partial t} + \operatorname{div}(\boldsymbol{F} - \boldsymbol{F}_v) = 0 \tag{1}$$

in which

$$\boldsymbol{f} = (\rho, \rho\boldsymbol{V}, \rho E)$$

$$\boldsymbol{F} = (\rho\boldsymbol{V}, \rho\boldsymbol{V} \times \boldsymbol{V} + p\boldsymbol{I}, \rho E\boldsymbol{V} + p\boldsymbol{V})$$

$$\boldsymbol{F}_v = [0, \tau + \tau_R, (\tau + \tau_R)\boldsymbol{V} - \boldsymbol{q} - \boldsymbol{q}_t]$$

In the preceding expressions, ρ, $\boldsymbol{V}$, E denote the density, the mean velocity, and the total energy per unit of mass, respectively. The flux densities $\boldsymbol{F}$ and $\boldsymbol{F}_v$ represent the convective and the dissipative terms, respectively.

Assuming a perfect gas, the static pressure p is given by the equation of state

$$p = (\gamma - 1)\rho\left(E - \frac{V^2}{2} - k\right)$$

where

$$\gamma = C_p/C_v$$

Using the Stokes hypothesis, the shear stress tensor τ and the heat flux vector $\boldsymbol{q}$ take the following forms:

$$\tau = -\tfrac{2}{3}\mu \operatorname{div}(\boldsymbol{V})\boldsymbol{I} + \mu(\nabla\boldsymbol{V} + \nabla\boldsymbol{V}^T)$$

$$\boldsymbol{q} = -\chi\nabla T$$

The molecular viscosity μ is given by Sutherland's law and the coefficient of thermal conductivity χ is computed by assuming a constant Prandtl number equal to 0.72.

The tensor τ_R and the vector $\boldsymbol{q}_t$ are then related to the velocity gradient and the temperature gradient by formulas analogous to the laminar expressions

$$\tau_R = -\tfrac{2}{3}(\rho k + \mu_t) \operatorname{div}(\boldsymbol{V})\boldsymbol{I} + \mu_t(\nabla\boldsymbol{V} + \nabla\boldsymbol{V}^T)$$

$$\boldsymbol{q}_t = -\frac{\mu_t C_p}{Pr_t}\nabla T$$

The turbulence kinetic energy k and the eddy viscosity coefficient μ_t are determined by the turbulence model, the turbulent Prandtl number Pr_t being assumed constant and equal to 0.9.

Turbulence Models

The algebraic mixing length turbulence model was initially proposed by Michel et al.[14] to compute two-dimensional boundary layers. With a mixing length concept, the scalar μ_t is expressed from the local mean flow properties. In the three-dimensional extension of the present model, the eddy viscosity μ_t is computed by the following equation:

$$\mu_t = \rho l^2 F^2 |\Omega|$$

where

$$\Omega = \operatorname{curl}(\boldsymbol{V})$$

The mixing length is given by

$$l = 0.085\delta \tanh\left[\frac{Kd}{0.085\delta}\right]$$

with $K = 0.41$. In the preceding expression, d denotes Buleev's modified distance which takes into account the influence of several walls in the case of corner flows. Finally, δ is a modified boundary-layer thickness (for details, see Ref. 11).

The viscous sublayer damping function F is given by

$$F(z) = 1 - \exp\left[-\frac{z}{26K}\right]$$

where

$$z = \rho l^2 \frac{\mu + \mu_t}{\mu^2}|\Omega|$$

These expressions lead to an implicit equation of the form $\mu_t = f(\mu_t)$ which is solved by a fixed-point method. The turbulence kinetic energy is taken equal to zero in the present application.

The transport equation model is the well-known low-Reynolds-number Jones–Launder $[k, \epsilon]$ model which uses the following equations for the turbulence kinetic energy k and its dissipation rate ϵ (Ref. 15):

$$\frac{\partial \boldsymbol{g}}{\partial t} + \operatorname{div}(\boldsymbol{G} - \boldsymbol{G}_v) = \boldsymbol{S}$$

where

$$\boldsymbol{g} = (\rho k, \rho\epsilon), \qquad \boldsymbol{G} = (\rho k \boldsymbol{V}, \rho\epsilon \boldsymbol{V})$$

$$\boldsymbol{G}_v = \left[\left(\mu + \frac{\mu_t}{\alpha_k}\right)\nabla(k), \left(\mu + \frac{\mu_t}{\alpha_\epsilon}\right)\nabla(\epsilon)\right]$$

$$\boldsymbol{S} = \left(P_k - \rho\epsilon - D, C_{\epsilon 1} f_1 \frac{\epsilon}{k} P_k - C_{\epsilon 2} f_2 \rho \frac{\epsilon^2}{k} + E\right)$$

In these expressions $P_k = \boldsymbol{\tau}_R : \nabla \boldsymbol{V}$ is the production term in the turbulence kinetic energy equation, and D and E are the wall terms added to the k and ϵ equations, respectively. These terms are written according to the classical formulas as

$$D = 2\mu[\nabla\sqrt{k}]^2, \qquad E = \frac{2\mu\mu_t}{\rho}\left[\frac{\partial^2 V}{\partial n^2}\right]^2$$

where $\boldsymbol{n}$ represents the unit vector normal to the wall.

The eddy viscosity is given by:

$$\mu_t = C_\mu f_\mu \rho(k^2/\epsilon)$$

The f functions are expressed as follows:

$$f_1 = 1, \qquad f_2 = 1. - 0.3\exp\left(-Re_t^2\right)$$

$$f_\mu = \exp\left\{-\frac{2.5}{[1 + (Re_t/50)]}\right\}$$

and the turbulence Reynolds number is defined as

$$Re_t = \frac{\rho k^2}{\mu\epsilon}$$

Use of the turbulence Reynolds number to express the damping functions ensures a correct behavior in separated zones.

The values adopted for the different constants of the model are $C_\mu = 0.09$, $C_{\epsilon 1} = 1.55$, $C_{\epsilon 1} = 2.$, $\alpha_k = 1.0$, and $\alpha_\epsilon = 1.3$. The following boundary conditions are imposed at the wall: $k = 0$ and $\partial\epsilon/\partial\boldsymbol{n} = 0$. In fact, k is set equal to a small value to avoid divisions by zero. It is now generally agreed that the condition $\epsilon = 0$ (prescribed in the classical Jones–Launder model) is not physically correct. It has been demonstrated by an asymptotic analysis method corroborated by a DNS calculation[16] that, in reality, ϵ reaches an important value at the wall.

Numerical Method

The numerical method uses an explicit, centered finite difference scheme applied to a finite volume approach on a structured mesh.[6] The mean flow and the turbulent transport equations are both discretized by using a two-step Lax–Wendroff scheme.

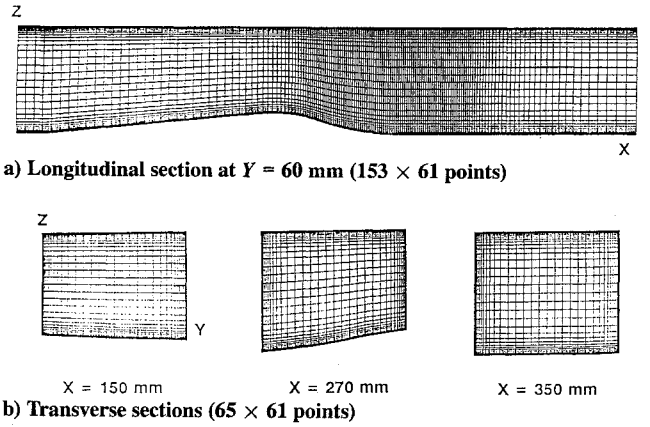

a) Longitudinal section at Y = 60 mm (153 × 61 points)

b) Transverse sections (65 × 61 points)

Fig. 2 Computational mesh.

Considering the turbulent transport equation $\boldsymbol{g}$, the solution $\boldsymbol{g}^{(n+1)}$ at time $t^{(n+1)} = t^{(n)} + \Delta t$ is computed by the following time discretization:

$$\boldsymbol{g}^{(n+\frac{1}{2})} = \boldsymbol{g}^{(n)} - \tfrac{1}{2}\Delta t \operatorname{div}\left[\boldsymbol{G}^{(n)} - \boldsymbol{G}_v^{(n)}\right] + \tfrac{1}{2}\Delta t \boldsymbol{S}^{(n)}$$

$$\boldsymbol{g}^{(n+1)} = \boldsymbol{g}^{(n)} - \Delta t \operatorname{div}\left[\boldsymbol{G}^{(n+\frac{1}{2})} - \boldsymbol{G}_v^{(n)}\right] + \Delta t \boldsymbol{S}^{(n+\frac{1}{2})}$$

The same relations are used for the mean flow equations, S being equal to zero. The dissipation terms are taken into account according to Thommen's idea. The space discretization of the divergence terms at each time step is performed by using an integral contour formulation. The source terms are evaluated at each step of the predictor-corrector scheme at the centers and at the nodes of the basic cells, respectively. A numerical viscosity is added to ensure the stability of the scheme and to correctly capture the flow discontinuities in the inviscid flow regions.

In the present application, the computational domain extends from $X = -30$ to 560 mm (see Fig. 2). Grid interpolation is made on surfaces constructed between the lower wall bearing the bump and the flat top wall. The number of grid points is equal to 606, 645, with 153 points along the X direction, 65 points in the Y direction, and 61 points in the Z direction, normal to the wall bearing the bump. High refinement is introduced near the walls to properly resolve the dissipative layers. The point closest to the wall is at a reduced ordinate Y^+ approximately equal to 3 in the boundary layer, upstream and downstream of the interaction region.

In the entrance section of the domain, the direction of the velocity is assumed parallel to the X axis. In the exit section, the static pressure was adjusted to obtain the experimental location of the leading oblique shock (Γ_1) at convergence (see subsequent section). These boundary conditions are complemented by characteristic relations allowing the determination of the other variables. At the wall a no-slip condition is applied. The mean flow calculation is initialized from an inviscid one-dimensional flow with a shock approximately located at the experimental position. The turbulence kinetic energy k is initialized from values of μ_t determined by a mixing-length hypothesis making Bradshaw's assumption. Then initial values of the dissipation rate ϵ are deduced by assuming that the production of turbulence is equal to its dissipation.

Presentation of Results

Surface Flow Properties

Skin-Friction Line Patterns

Interpretation of the surface flow patterns is based on the critical point theory.[17,18] This theory introduces singular points in the skin-friction line pattern (nodes, foci, saddle points) and special lines, called separatrices, which are defined as skin-friction lines passing through a saddle point. From a physical point of view, a separatrix (S) is either a separation line or an attachment line, according to the flow behavior in its vicinity.[9]

The photographs in Fig. 3 show the surface flow visualizations performed on the four channel walls by using an oil-flow technique.

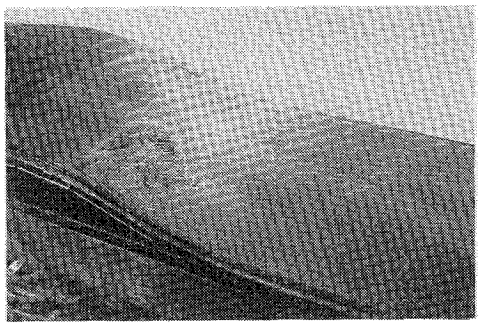

a) Flow on the wall bearing the bump

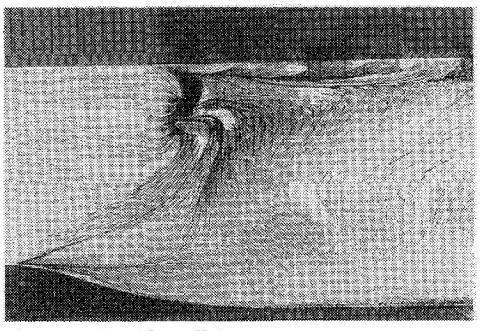

b) Flow on the side wall A

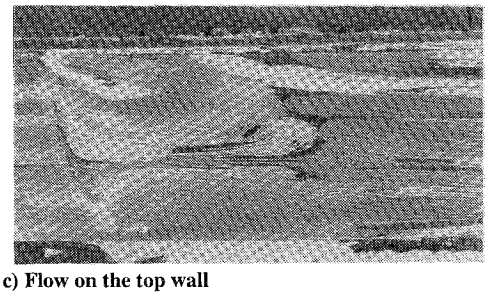

c) Flow on the top wall

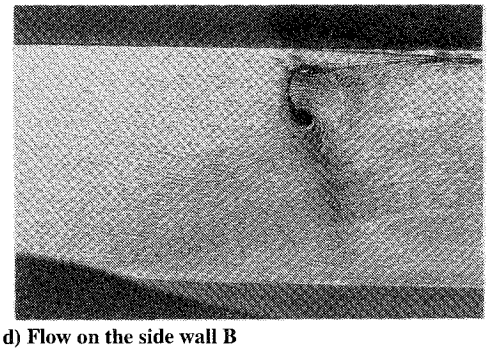

d) Flow on the side wall B

Fig. 3 Surface flow visualizations.

These pictures reveal the organization of the surface flow pattern and allow an identification of the main separation and attachment lines. The diagrams in Fig. 4, which have been established from a careful inspection of the visualizations, give a topological interpretation of the skin-friction line patterns on the four faces of the channel. Here we will only examine the flow over the bump (see Fig. 4a). Its skin-friction line pattern contains one focus F_1 around which rolls up the separation line (S_1), emanating from the half-saddle point C_1 located at the junction between the lower wall and sidewall A. A second half-saddle point C_2 exists downstream of C_1 through which passes the separator (S_2), which is an attachment line. The skin-friction lines coming from upstream that are flowing between (S_2) and sidewall A wind around F_1 into which they disappear; those located above (S_2) continue their way downstream. The spirals winding around F_1 are the traces on the lower wall of a tornado-like vortex escaping into the flow with the separation line (S_1) being the origin of a separation surface that winds around the axis of the vortex structure. A similar description of the wall patterns in terms of singular points and separation/attachment lines can be made for the other faces of the channel, care being taken to insure continuity of the patterns at the crossing of the corner lines between adjacent walls.

The skin-friction line patterns deduced from the Navier–Stokes calculation using the $[k, \epsilon]$ model are also shown in Fig. 4, in correspondence with the experimental observations. There is a close similarity between the computed and the experimental patterns, although some differences are observed. Thus, considering the lower wall which bears the bump, the calculation clearly exhibits focus F_1 as the two half-saddle points C_1 and C_2. The corresponding separatrices (S_1) and (S_2) can also be identified. The major differences lie in the existence of a complex structure close to the upper corner line, which is not detected by the experimental observations, and in a convergence process of the skin-friction lines taking place in the upstream part of the domain, which is not confirmed by the surface flow visualization. The major features of the calculated pattern for face A are in remarkable agreement with experiment. Differences exist downstream of the separation line (S_3), the observed pattern being more complex than the computed one.

The essential features of the top wall pattern are predicted, but the scale of the computed phenomena is contracted, the distance between the separation line (S_9) and the attachment line (S_{11}) being shorter in the calculation than in the experiment. Relatively large differences are noticed on face B where the two-vortex structure seen in the experiment is not obtained.

The comparisons lead to the following comments.

1) Skin-friction line patterns in such complicated flows are extremely sensitive to any slight change in the configuration. Thus, a nearly indetectable modification of the outer flow can lead to a major reorganization of the surface pattern with a jump in the number of critical points. In these conditions, small differences coming from the imperfection of the turbulence models can be dramatically amplified at the level of the skin-friction line pattern.

2) The oil film deposited on the walls to visualize the skin-friction lines can affect the flow in the immediate vicinity of the surface, its thickness being not negligible.

3) Computation of the skin-friction lines from the skin-friction vector field by a trajectography technique is delicate in some regions of the field where vector directions vary rapidly.

Wall Pressure Distributions

Some pressure distributions on the four channel walls are plotted in Fig. 5. These distributions first exhibit a rapid expansion in the upstream converging part of the channel. On the bump, the flow goes supersonic, reaching a maximum Mach number of 1.75 as denoted by the pressure measured at the wall. For the upper and lower walls, clear differences exist between the three distributions. Close to face A ($Y = 15$ mm), one observes a steep pressure rise terminating the expansion process. This rise, which denotes the existence of a shock, is followed by a well-defined plateau. Farther downstream, a more progressive compression takes place, the expansion at the extremity of the domain being caused by the acceleration induced by the second throat. The shape of the pressure curves is typical of a transonic interaction with shock-induced separation, the rapid pressure rise being associated with the separation process, denoted by the separation line (S_1) observed in Fig. 4a, and the pressure plateau with the large vortical structure extending between C_1 and C_2.

In the median plane ($Y = 60$ mm), the first pressure rise is less rapid and the plateau has disappeared. A small pressure jump is observed at X close to 300 mm. In the immediate vicinity of face B ($Y = 105$ mm), the compression which follows the expansion on the first part of the bump is now progressive, no separation shock being observed. This pressure distribution has to be placed in correspondence with the surface pattern observed in the vicinity of face B (see Figs. 4a and 4d); in this part of the flow, the wall pattern is free of critical points and separatrices. In the upstream part of the channel, where the flow is accelerating, the two Navier–Stokes calculations are in excellent agreement with experiment. Considering

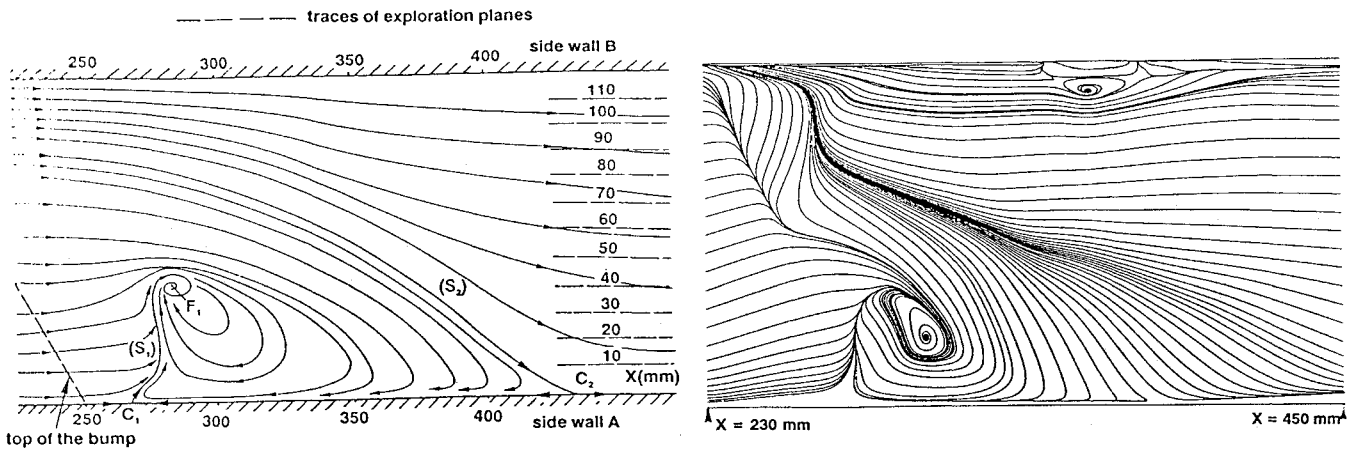

a) Flow on the wall bearing the bump

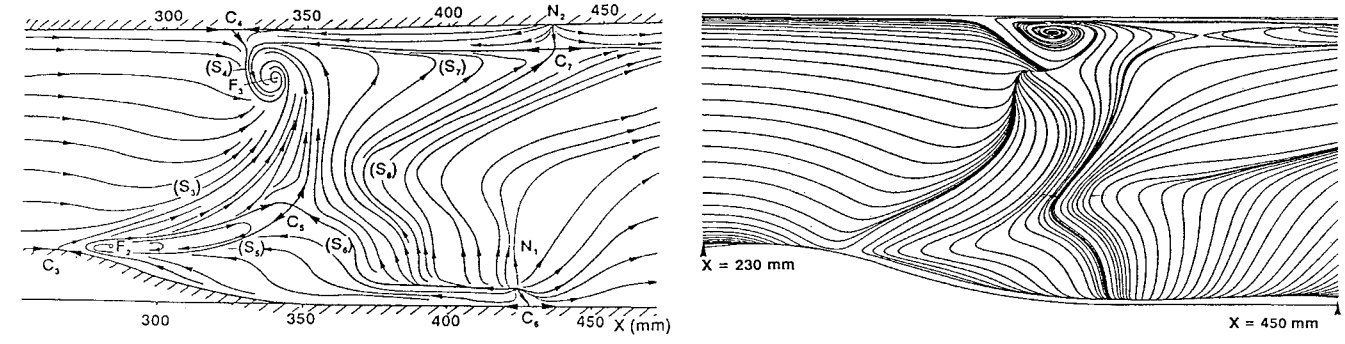

b) Flow on the side wall A

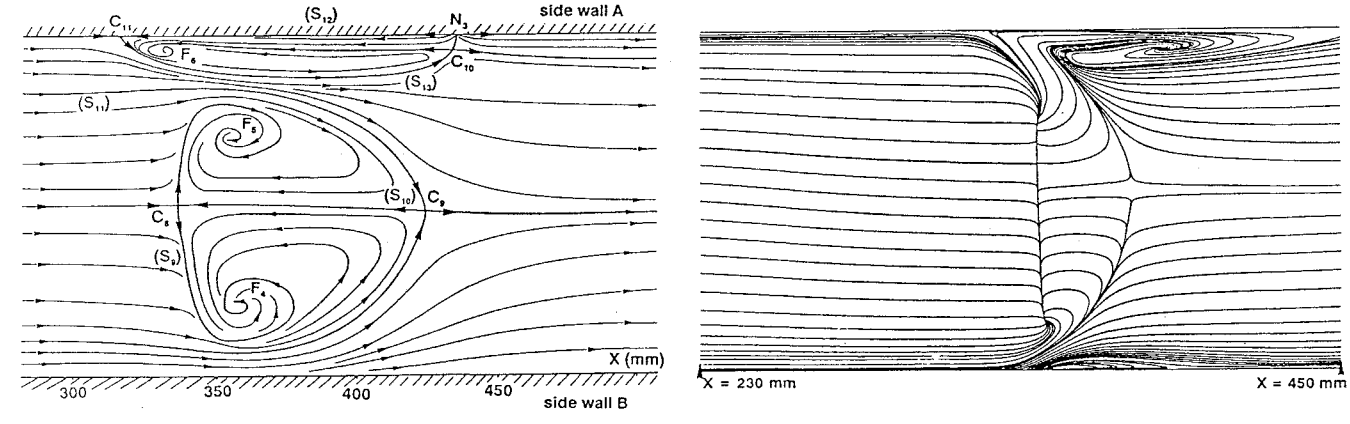

c) Flow on the top wall

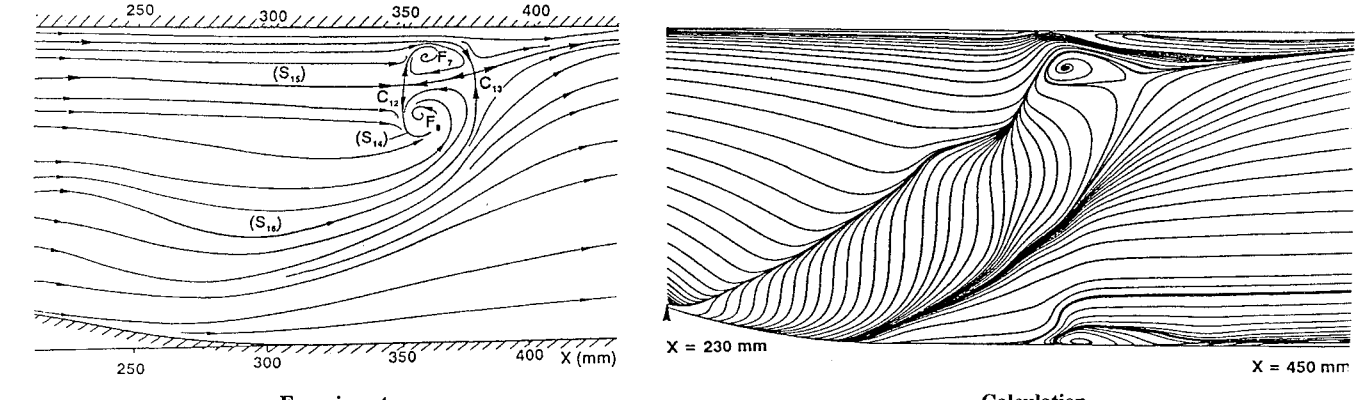

Experiment Calculation

d) Flow on the side wall B

Fig. 4 Topological interpretation of the surface flow visualizations and computed skin-friction line patterns.

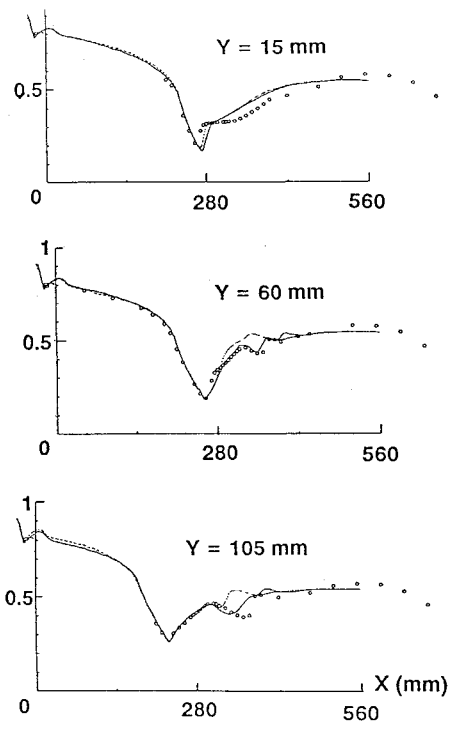

a) On the wall bearing the bump

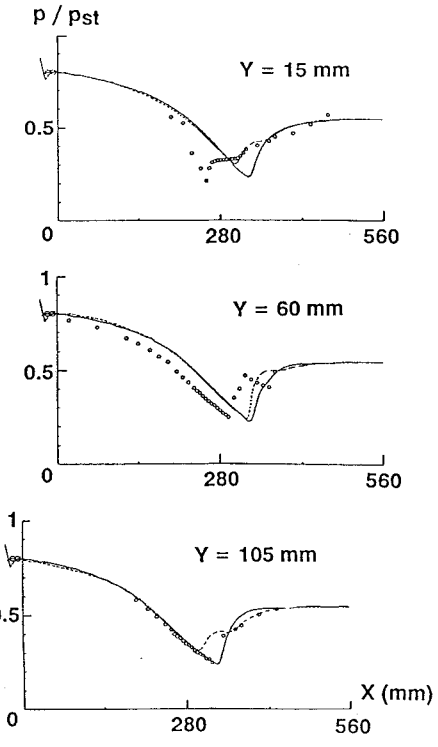

b) On the top wall

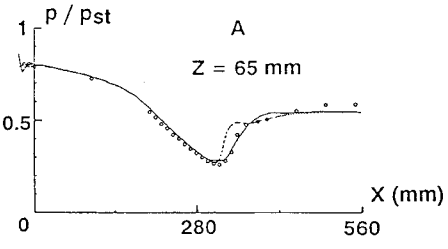

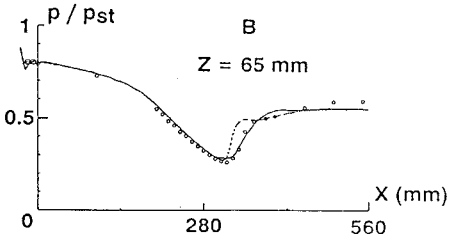

c) On the side walls

Fig. 5 Wall pressure distributions: o o o o experiment; - - - - algebraic model; ——— $[k, \epsilon]$ model.

the parts of the flow where viscous effects are important, the calculation using the $[k, \epsilon]$ turbulence model is in very good agreement with experiment, especially along lines $Y = 60$ and 105 mm. Major discrepancies exist close to side wall A where the pressure plateau is not captured by either calculation. The algebraic model which is comparable to the $[k, \epsilon]$ model in section $Y = 15$ mm leads to poor results in the other parts of the channel.

Mean Flow Field Properties

Mach Number Distributions in Longitudinal Planes.

The experimental values of the Mach number have been determined from the mean velocity vector measurements made with the LDV system assuming a uniform stagnation temperature, even in the dissipative regions. This approximation is well verified in transonic adiabatic flows.

The computed and experimental Mach number contours relative to planes located at $Y = 10$, 30, 60, and 90 mm are shown in Figs. 6a–6d. The plane $Y = 10$ mm traverses the interacting boundary layer of face A which explains the spreading of the Mach number distributions (peaks in the experimental Mach number contours near the bump are due to erroneous values). There is a close similarity between the computed and measured fields, although the bundle of Mach number contours close to the top wall is thicker in the computations than in the experiment. In planes located at $Y = 30$ and 60 mm, a lambda shock pattern is clearly visible. This pattern consists of a leading oblique shock (Γ_1); and a nearly normal shock (Γ_2), occupying about half of the channel in its upper part; a leg (Γ_3), consisting of a weak shock hardly discernible in the experiment (the important thickening of the shocks in the experimental plottings is due to the spacing of the measurement points). In plane $Y = 30$ mm, the tracings reveal the large region of separated flow starting from the foot of shock (Γ_1), which was already detected from the surface flow visualizations and the pressure distributions. This zone disappears completely when one tends toward face B. A separated zone induced by shock (Γ_2) is also clearly visible near the top wall, in planes $Y = 30$, 60, and 90 mm. At $Y = 90$ mm the oblique shock (Γ_1) is replaced by a continuous compression.

The calculation using the $[k, \epsilon]$ model reproduces faithfully all of the flow features. In particular, this model allows an accurate prediction of the origin of the interaction produced by the shock waves, which is not the case of the algebraic model (see Fig. 6c). In addition, the algebraic model tends to overpredict the thickening of the dissipative region caused by the shock wave/boundary layer interactions.

Longitudinal Velocity Profiles

A more objective validation of the accuracy of these calculations is provided by a comparison of the velocity distributions across the channel. Thus, Fig. 7 shows the profiles of the streamwise velocity component U in the median plane $Y = 60$ mm for nine Xwise stations. The first profile at $X = 290$ mm crosses the leading oblique shock (Γ_1) close to the bump. Farther downstream, the trace of (Γ_1), well visible on the profiles, moves away from the lower surface. Section $X = 350$ mm nearly coincides with the quasinormal shock (Γ_2) which explains a certain scatter in the measured values. Downstream, the exploration lines traverse the subsonic part of the flow.

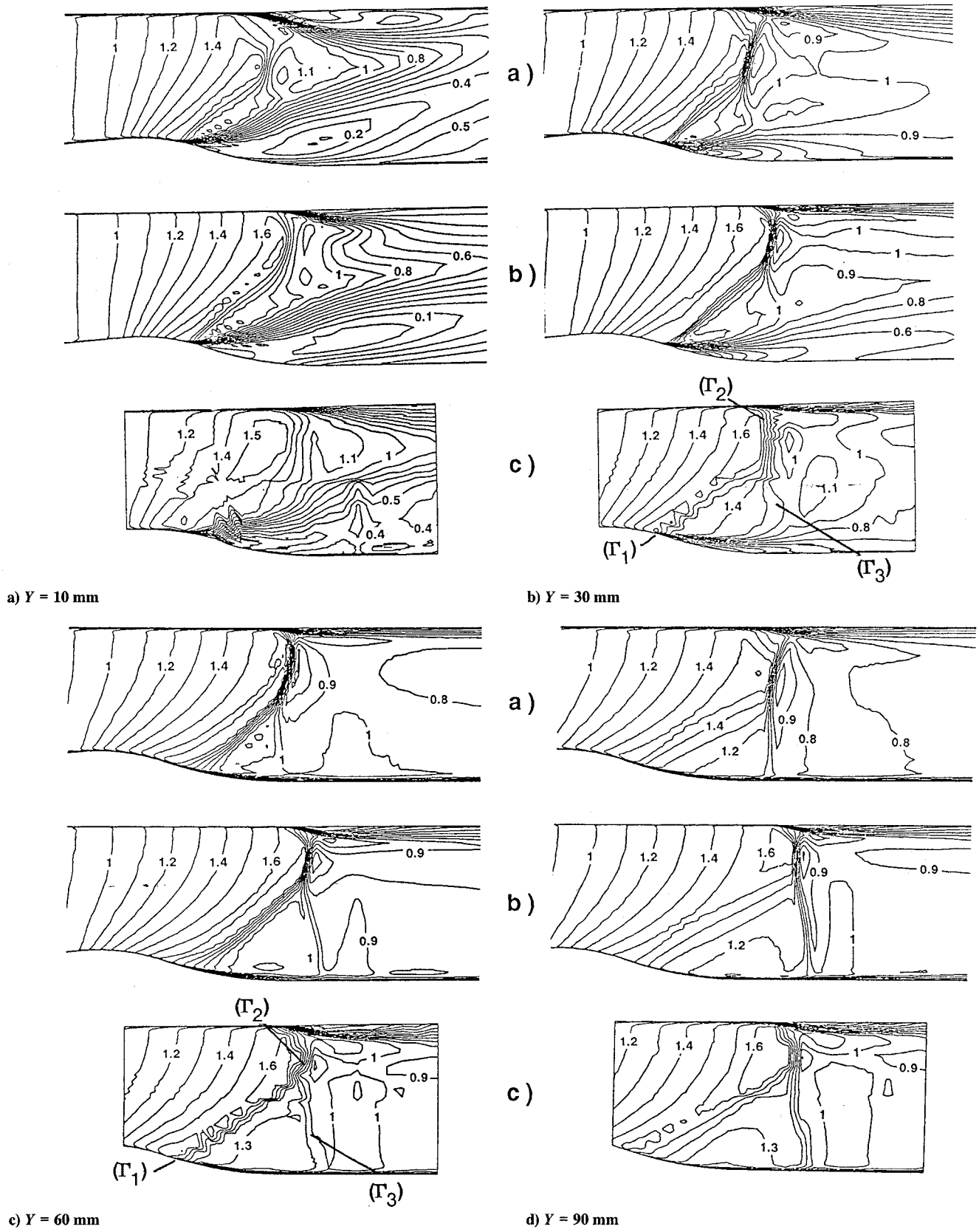

a) Y = 10 mm

b) Y = 30 mm

c) Y = 60 mm

d) Y = 90 mm

Fig. 6 IsoMach lines in longitudinal planes, intervals ΔM = 0.1: a) algebraic model, b) $[k, \epsilon]$ transport equation model, and c) experiment.

The interaction between the top wall boundary layer and shock (Γ_2) gives rise to an important thickening of the dissipative layer. Close to the wall, negative values of the U component are observed at X = 350 mm, i.e., just downstream of the foot of (Γ_2). The region of reversed flow extends down to X = 410 mm where it vanishes. This region of backflow is in agreement with the pattern observed at the wall (see Fig. 4c), its origin being coincident with the separation line (S_9) and its resorbtion with the attachment line (S_{11}).

In general, there is a good agreement between the computed and the measured profiles, the best results being obtained with the $[k, \epsilon]$ model. However, relaxation of the boundary layer downstream of

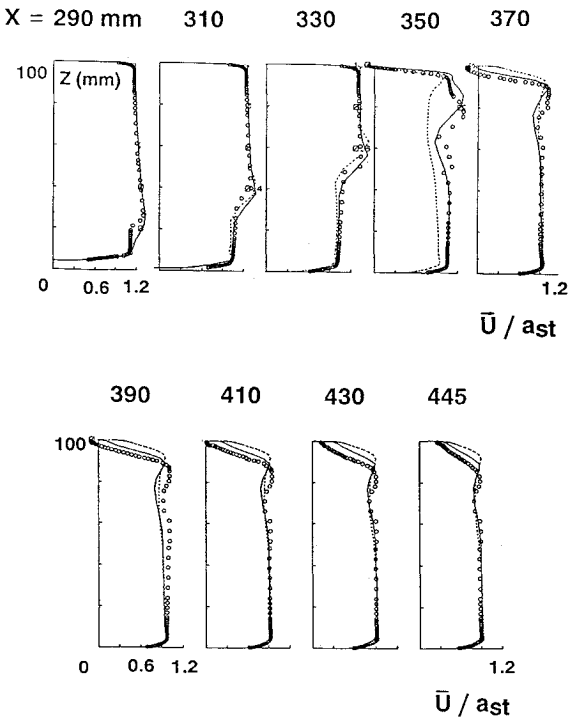

Fig. 7 Mean streamwise velocity profiles in the longitudinal plane at Y = 60 mm: o o o o experiment; - - - - algebraic model; ——— $[k, \epsilon]$ model.

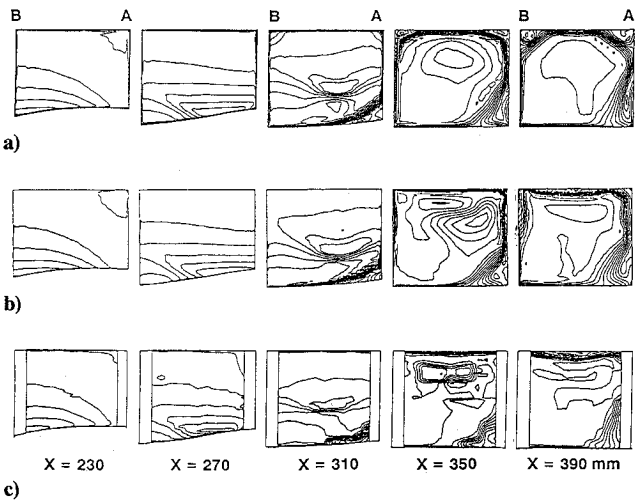

Fig. 8 IsoMach lines in transverse planes: a) algebraic model, b) $[k, \epsilon]$ transport equation model, and c) experiment.

the strong interaction taking place on the upper wall, at the foot of shock (Γ_2), is ill predicted, even by the transport equation model. As a general rule, most turbulence models predict a too fast relaxation process. In the present case, the computed profile at $X = 390$ mm is fully attached, whereas the measured profile still has a backflow region. Also, the thickness of the relaxing boundary layer is underpredicted.

Flow in Transverse Planes

The flow in the (Y, Z) planes is represented in Fig. 8 by tracings of the Mach number contours. The explored region extends from $Y = 10$ to 110 mm in the spanwise direction, the use of the LDV system close to the lateral glass windows being difficult because of important parasitic stray light.

The first station at $X = 230$ mm is located upstream of the shock system. There, due to the strong acceleration of the flow,

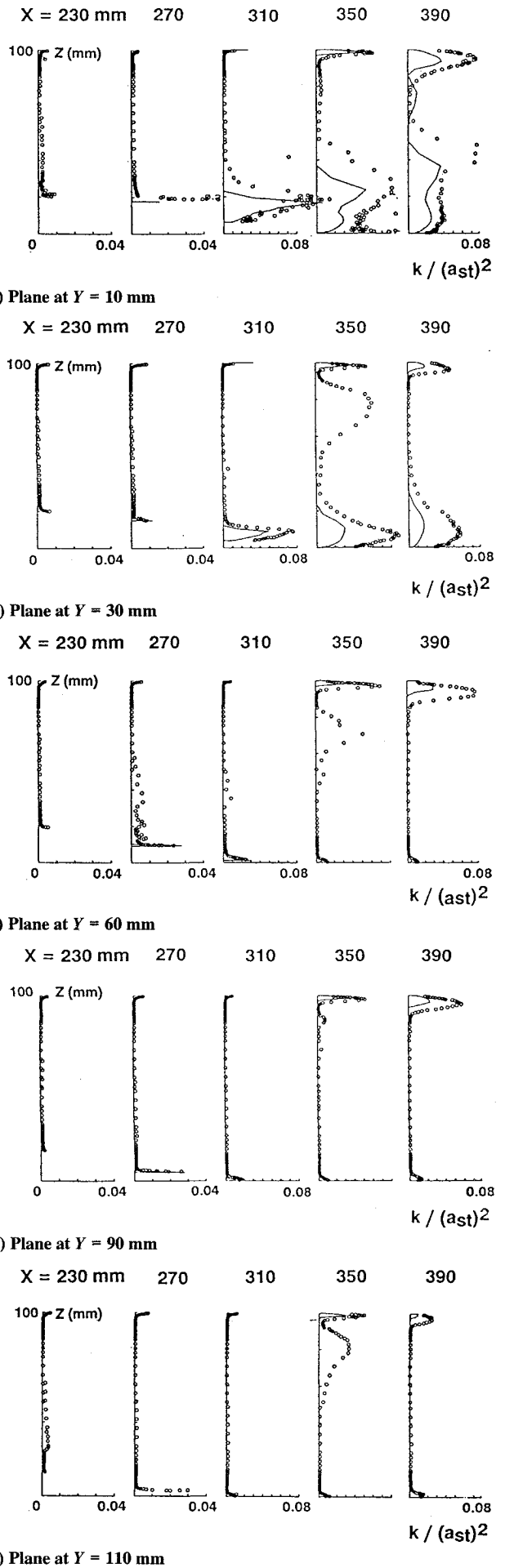

Fig. 9 Turbulence kinetic energy profiles.

viscous effects are extremely weak and so the boundary layers are barely visible. The second station at $X = 270$ mm nearly coincides with the origin of shock (Γ_1), and so the viscous effects are still unimportant. The third plane, at $X = 310$ mm, crosses shock (Γ_1) but is upstream of the nearly normal shock (Γ_2). A region of intense interaction is visible in the vicinity of the corner line between the lower wall and the side wall A. There, the boundary layer undergoes a rapid and important thickening which corresponds to the vortical structure originating at the combination of the two half-saddle points $C_1 + C_2$ (see Figs. 4a and 4b). The algebraic turbulence model tends to exaggerate this thickening of the viscous layer, the results given by the $[k, \epsilon]$ model being closer to the experiment.

The plane $X = 350$ mm is very close to the transverse plane containing the strong shock (Γ_2), which can explain some erratic behavior of the isoMach lines in the central part of the channel. The thickening of the top wall boundary layer due to the interaction with (Γ_2) is well visible on the three tracings, as is also the interaction taking place on the side wall A. The last plane, $X = 390$ mm, is well downstream of the shock system. One notes the important thickness of the top wall boundary layer and the large dissipative region still existing at the corner line between the lower wall and the side wall A. In fact, as shown by the skin-friction line patterns of Fig. 4, this transverse plane still crosses the vortical flow comprised between the saddle point ($C_1 + C_2$) and the node ($N_2 + N_3$).

Turbulence Properties

The profiles of the turbulence kinetic energy k (normalized by the square of the sound velocity for stagnation conditions a_{st}^2) in five longitudinal planes are shown in Fig. 9, the experimental values of k being compared to the values given by the $[k, \epsilon]$ model. At station $X = 270$ mm, we note a rise in k close to the lower wall. This peak is produced by the start of the interaction between the bump boundary layer and the oblique shock (Γ_1). In the vicinity of the side wall A (plane $Y = 10$ mm), very high levels of k are measured downstream of $X = 270$ mm (note the change in the scale for profiles beyond $X = 270$ mm). These important values of the turbulence kinetic energy are correlated with the strong interaction taking place on the side wall A in this region. The $[k, \epsilon]$ model tends to reproduce this behavior, although the predicted levels are substantially below the experimental results. This defficiency is a well-known tendency of the Jones–Launder model.

In the same way, the rise in turbulence occurring near the top wall because of the interaction produced by the shock (Γ_2) is underpredicted, especially in the downstream part of the interaction domain. As already mentioned, the classical turbulence models predict a too fast relaxation process behind a region of strong interaction, thus a too rapid fall in the turbulence levels and a too rapid filling of the mean velocity profiles. The measured profiles located at $X = 350$ mm exhibit a bump in the k distribution at some distance from the top wall. This phenomenon, which is completely ignored by the calculation, is in fact due to a slight oscillation of the shock (Γ_2).

Conclusion

The flow induced by a swept bump mounted on the lower wall of a three-dimensional transonic channel has been analyzed on the basis of surface pressure measurements, surface flow visualizations, and field measurements by a three-component LDV system. These tests have revealed a complex organization of the skin-friction line patterns which contain several separation/attachment lines and foci which are the traces on the walls of vortices escaping into the outer flow. Field explorations have given precise information on the shock pattern associated with the viscous-inviscid interactions taking place on the four faces of the channel. They also made it possible to describe in detail the viscous layers which contain extended separated regions, especially on the lower and upper walls.

The same flow has been computed by a code solving the full time-averaged Navier–Stokes equations by an explicit centered finite volume approach. Two turbulence models have been considered: the first one is an algebraic model using the mixing length concept, and the second one is the Jones–Launder $[k, \epsilon]$ transport equation model. Both models lead to a faithful prediction of the essential features of the flow; in particular, the shock pattern forming in the channel is well predicted. However, the $[k, \epsilon]$ model shows a clear superiority in the prediction of the behavior of the interacting dissipative layers. Thus, the main critical points and separation/attachment lines of the skin-friction line patterns are predicted, although some discrepancies exist which can be due, in part, to experimental uncertainty. The wall pressure distributions and the mean velocity profiles across the boundary layer, computed with the $[k, \epsilon]$ model are in fair agreement with experiment. However, the variation of the turbulent quantities is still far from being correctly predicted. In particular, even the transport equation model is not capable of accounting for the slow relaxation of turbulence downstream of the interaction regions.

Acknowledgment

This study has been performed with the financial support of the Direction des Recherches et Etudes Techniques of the French Ministry of Defense. The authors are very grateful to the Laser Measurement Team of the ONERA Experimental Aerodynamics Branch who executed the field measurements.

References

[1]Délery, J., and Marvin, J. G., "Shock Wave/Boundary Layer Interactions," AGARDograph No. 280, June 1986.

[2]Le Balleur, J.-C., "Viscous Inviscid Interaction Solvers and Computation of Highly Separated Flows," *Studies of Vortex Dominated Flows*, Springer-Verlag, Berlin, 1987, Chap. 3, pp. 158–192.

[3]Inger, G. R., and Mason, W. H., "Analytical Theory of Transonic Normal Shock Wave/Turbulent Boundary Layer Interaction," *AIAA Journal*, Vol. 14, No. 9, 1976, pp. 1266–1272.

[4]Bohning, R., and Zierep, J., "The Normal Shock at a Curved Wall in the Viscous Case," *Symposium Transsonicum II*, Springer-Verlag, Berlin, 1976, pp. 237–243.

[5]Viegas, J. R., and Horstman, C. C., "Comparison of Multiequation Turbulence Models for Several Shock-Boundary Layer Interaction Flows," *AIAA Journal*, Vol. 17, No. 8, 1979, pp. 811–820.

[6]Couaillier, V., Veysseyre, P., and Vuillot, A.-M., "3-D Navier–Stokes Computations in Transonic Compressor Cascades," *Proceedings of the 10th International Symposium on AirBreathing Engines,* edited by F. S. Billig, AIAA, Washington, DC, 1991.

[7]Benay, R., Coët, M.-C., and Délery, J., "A Study of Turbulence Modelling in Transonic Shock Wave-Boundary Layer Interactions," *Turbulent Shear Flows 6*, Springer-Verlag, Berlin, 1989, pp. 194–214.

[8]Peake, J., and Tobak, M., "Three-Dimensional Interactions and Vortical Flows with Emphasis on High Speeds," AGARDograph No. 252, 1980.

[9]Délery, J., "Physics of Vortical Flows," *Journal of Aircraft*, Vol. 29, No. 5, 1992, pp. 856–876.

[10]Benay, R., Délery, J., and Pot, T., "Analyse expérimentale de l'écoulement dans un canal transsonique tridimensionnel," *La Recherche Aérospatiale*, No. 1986-6, Nov.–Dec. 1986, pp. 399–414 (French and English editions).

[11]Cambier, L., and Escande, B., "Calculation of a Three-Dimensional Shock Wave-Turbulent Boundary Layer Interaction," *AIAA Journal*, Vol. 28, No. 11, 1990, pp. 1901–1908.

[12]Pot, T., Délery, J., and Quélin, C., "Interaction onde de choc-couche limite dans un canal transsonique tridimensionnel. Nouvelles expériences," ONERA, Rept. No. 92/7078AY116A, Châtillon, France, Feb. 1991.

[13]Boutier, A., d'Humières, C., and Soulevant, D., "Three-Dimensional Laser Velocimetry: a Review," 2nd International Symposium on Application of Laser Anemometry to Fluid Mechanics, Lisbon, Portugal, July 1984, and ONERA, TP 1984-43, 1984.

[14]Michel, R., Quémard, C., and Durant, R., "Application d'un schéma de longueur de mélange à l'étude des couches limites turbulentes d'équilibre," ONERA, Note Technique No. 154, Châtillon, France, 1969.

[15]Jones, W. P., and Launder, B. E., "Prediction of Laminarization with a Two-Equation Model of Turbulence," *International Journal of Heat and Mass Transfer*, Vol. 15, Feb. 1972, pp. 301–314.

[16]Mansour, N. N., Kim, J., and Moin, P., "Near-Wall $[k, \epsilon]$ Turbulence Modeling," *AIAA Journal*, Vol. 27, No. 8, 1988, pp. 1068–1073.

[17]Poincaré, H., "Les points singuliers des équations différentielles," C. R., Académie des Sciences, Paris, T. 94, Feb. 13, 1882, pp. 416–418.

[18]Legendre, R., "Lignes de courant d'un écoulement permanent. Décollement et séparation," *La Recherche Aérospatiale*, No. 1977-6, Nov.–Dec. 1977, pp. 327–335.